

Photonic Hybrid State Entanglement Swapping using Cat State Superpositions

Ryan C. Parker^{1*}, Jaewoo Joo², Timothy P. Spiller¹

¹York Centre for Quantum Technologies, Department of Physics, University of York, York, YO10 5DD, U.K.

²School of Mathematics and Physics, University of Portsmouth, Portsmouth, PO1 3QL, U.K.

We propose the use of hybrid entanglement in an entanglement swapping protocol, as means of distributing a Bell state with high fidelity to two parties, Alice and Bob. The hybrid entanglement used in this work is described as a discrete variable (Fock state) and a continuous variable (cat state superposition) entangled state. We model equal and unequal levels of photonic loss between the two propagating continuous variable modes, before detecting these states via a projective vacuum-one-photon measurement, and the other mode via balanced homodyne detection. We investigate homodyne measurement imperfections, and the associated success probability of the measurement schemes chosen in this protocol.

We show that our entanglement swapping scheme is resilient to low levels of photonic losses, as well as low levels of averaged unequal losses between the two propagating modes, and show an improvement in this loss resilience over other hybrid entanglement schemes using coherent state superpositions as the propagating modes. Finally, we conclude that our protocol is suitable for potential quantum networking applications which require two nodes to share entanglement separated over a distance of 5 – 10 km, when used with a suitable entanglement purification scheme.

1 Introduction

The future of large-scale quantum communications will almost certainly involve distribution and manipulation of entangled pairs of photons within a quantum network; such a quantum network is likely to include small clusters of quantum processors (perhaps in a local network of quantum computers) which may require shared entanglement, and could then be connected to other network clusters, potentially via satellite communications [1–3]. However, despite the undeniably useful non-classical properties which entanglement-based quantum systems offer (such as for quantum key distribution [4–7], quantum secret sharing [8–10], quantum repeaters [11–14], quantum computing [15–18] and quantum teleportation [19–22]), entanglement is a highly fragile resource, and breaks down rapidly in the presence of noise and losses [23].

One particularly useful proposal for circumventing the intrinsic fragility of distributing entangled photons around a quantum network is by performing entanglement swapping (ES). In ES, there exist two parties, Alice and Bob, each of whom begin the protocol with a separately entangled pair of photons, AB and CD respectively. They each send half of their entangled pair (i.e. modes B and D) to a central location, where these propagating modes are mixed at a 50:50 beam-splitter, before subsequently being measured, as described in the schematic of

Fig. 1. This mixing and measurement step is key to ES, as it causes projection of the states in modes B and D , thus projecting modes A and C into an entangled state.

This distributed entanglement, now shared between modes A and C , can then be used for further quantum communications and quantum computational purposes. Moreover, performing ES to share entanglement enhances the secrecy and security of the post-entangled state shared between Alice and Bob; if an adversary, Eve, were to measure modes B and D , she gains no useful information on states A and C , and in fact by carrying out this measurement Eve has actually *assisted* Alice and Bob in sharing an entangled state [24].

This in fact is a form of measurement-device independence [25–27], and is a direct consequence of the monogamy of entanglement: if Alice and Bob share an entangled state of high fidelity, then Eve must be disentangled from this state. As a result of this, Alice and Bob need not trust the source of entanglement. However, Eve, as the source of entanglement, could simply deny service, and there is no way to circumvent this form of attack.

ES, first performed experimentally in 1993 [28], has since been executed with discrete variables (DVs) [29–31], and also with continuous variables (CVs) [32,33]. CV systems typically pose the advantage of high success probability, whereas DVs are often robust against lossy channels; hence, an advantage could be gained from using both CV and DV

*Current address: BT Research, Polaris House, Adastral Park, Ipswich, IP5 3RE, U.K.

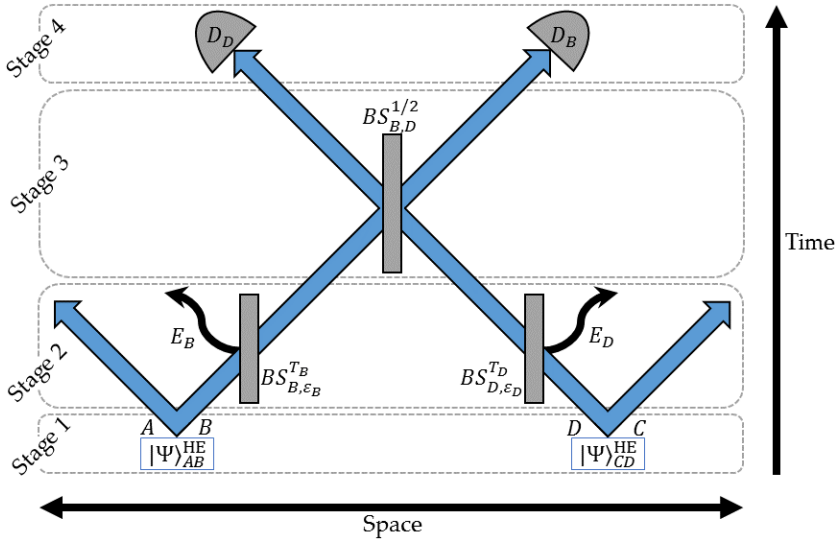


Figure 1: Schematic to represent the six channel system (in which the initial hybrid entangled states are denoted as $|\Psi_{AB}^{\text{HE}}\rangle$ and $|\Psi_{CD}^{\text{HE}}\rangle$) undergoing entanglement swapping. Modes A and C are the discrete variable post-entangled modes, and B and D are the propagating continuous variable modes. Losses are modelled through leakage of modes B and D into modes E_B and E_D respectively. The lossy modes B and D then meet at a 50:50 beam-splitter ($BS_{B,D}^{1/2}$) before subsequently being measured via a projective vacuum measurement and balanced homodyne detection (D_B and D_D , respectively).

states in what is referred to as a hybrid entanglement scheme [34], and will be investigated in this work. The practicality of using CVs is also worth noting; they are compatible with current standard optical telecommunication technologies, and so could be suitable for large-scale communication protocols [35, 36]. Both, DVs and CVs, have been extensively researched when used in entanglement swapping protocols together in the form of hybrid entanglement [37, 38], and have also been demonstrated experimentally [39].

In this work we present a new ES protocol based on hybrid entangled cat states. We show that we can produce a Bell state of high fidelity when allowing for low levels of photonic losses in the propagating CV (cat state superposition) modes, as well as allowing differences in the losses between the two propagating modes.

This paper is organised as follows: in Section 2 we introduce our proposed ES protocol, as well as our model for photonic losses in the propagating modes, and the detection methods used; we extend this model for loss, and include averaged unequal losses between modes B and D , in Section 3; in Section 4 we show that, following our proposed ES protocol, Alice and Bob can share a Bell state of high fidelity, when allowing for low levels of equal and unequal losses, as well as investigating homodyne measurement imperfections; we discuss the practicality of our protocol for distributing entanglement in a future quantum network in Section 5; our conclusions are given in Section 6.

2 The Entanglement Swapping Protocol

A space-time schematic describing the process of our proposed ES protocol, from initial hybrid entangled state generation through to detection, is given in Fig. 1, in which each arrow indicates a channel/mode. Within Fig. 1, the arrows illustrating modes A and C indicate a movement in space; this

is to represent the possibility that these modes may be sent on for further uses in quantum communications protocols or quantum computing, or perhaps even to a potential customer (or indeed separated customers), requiring an entangled pair of qubits.

We now discuss each stage of our proposed protocol, starting with the production of the initial hybrid entangled states, before moving on to discuss how we model photonic losses in the propagating modes, and our subsequent detection methods.

2.1 Hybrid States with Superposed Cats

Within this ES protocol, we propose the use of so-called *hybrid entangled* states. These quantum states are described as having entanglement shared between DV and CV degrees of freedom.

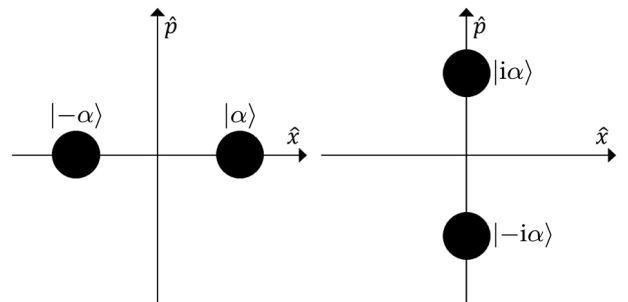


Figure 2: The position and momentum phase space (\hat{x} and \hat{p} respectively, where $\hat{x} = \frac{1}{2}(\hat{a} + \hat{a}^\dagger)$ and $\hat{p} = \frac{1}{2}(\hat{a}^\dagger - \hat{a})$), in which we have two even cat states, $\mathcal{N}_\alpha^+(|\alpha\rangle + |-\alpha\rangle)$ (left) and the phase-rotated $\mathcal{N}_\alpha^+(|i\alpha\rangle + |-i\alpha\rangle)$ (right).

Extensive experimental research has been carried out preparing various hybrid entangled states, and one such commonly investigated state is the $|\psi\rangle_{AB} = \frac{1}{\sqrt{2}}(|0\rangle_A |\alpha\rangle_B + |1\rangle_A |-\alpha\rangle_B)$ state, which shows bipartite hybrid entanglement between a qubit and a CV mode (commonly referred to as an entangled ‘‘Schrödinger cat state’’). This can be prepared in a multitude of ways, such as via use of polarisation photons, probabilistic heralded single

photon measurements and Hadamard gates [40], by relying on Kerr non-linearities [41–44], or by exploiting entangled polarisation qubits with a series of beam-splitters (BSs) and auxiliary modes [45]. In fact, previous work has investigated this particular hybrid state in the same ES protocol as followed in this work, demonstrating that this simple hybrid state is theoretically resilient to low levels of photonic losses [46,47].

2.2 Stage 1: Preparation of Hybrid Entanglement

In this work we consider hybrid entangled cat states, in which the CV components in the superposition are themselves cat states, as shown in Fig. 2.

Alice’s input quantum state to our proposed ES protocol is then described mathematically as follows:

$$|\Psi\rangle_{AB}^{\text{HE}} = \frac{\mathcal{N}_\alpha^+}{\sqrt{2}} [|0\rangle_A (|\alpha\rangle_B + |-\alpha\rangle_B) + |1\rangle_A (|i\alpha\rangle_B + |-i\alpha\rangle_B)], \quad (1)$$

in which $\mathcal{N}_\alpha^\pm = 1/\sqrt{2 \pm 2e^{-2\alpha^2}}$ is the normalisation of an even (or odd) cat state. We importantly note that, unless stated otherwise, α is real throughout this work. Furthermore, Bob’s hybrid state of modes C and D ($|\Psi\rangle_{CD}^{\text{HE}}$) is identical to that of Alice’s in modes A and B , as described in Eq. 1, and so our total quantum state at this stage is:

$$|\Psi\rangle_{ABCD}^{\text{HE}} = |\Psi\rangle_{AB}^{\text{HE}} \otimes |\Psi\rangle_{CD}^{\text{HE}}. \quad (2)$$

The hybrid states utilised in the protocol discussed here have increased complexity and thus require additional preparation steps, compared to the usual hybrid states. We therefore propose a sequence of quantum operations capable of producing such complex hybrid states, as the first stage of our protocol, as follows:

1. Begin with an initial product state of:

$$|\Psi\rangle_{AB} = \mathcal{N}_\alpha^+ [|0\rangle_A (|\alpha\rangle_B + |-\alpha\rangle_B)]. \quad (3)$$

2. Apply a Hadamard gate (\hat{H}) to mode A , such that $|0\rangle_A \xrightarrow{\hat{H}} \frac{1}{\sqrt{2}} (|0\rangle_A + |1\rangle_A)$. The state after this is then:

$$|\Psi\rangle_{AB} = \frac{\mathcal{N}_\alpha^+}{\sqrt{2}} [|0\rangle_A (|\alpha\rangle_B + |-\alpha\rangle_B) + |1\rangle_A (|\alpha\rangle_B + |-\alpha\rangle_B)]. \quad (4)$$

3. Finally, perform a conditional (controlled) $\frac{\pi}{2}$ rotation on mode B , such that when the qubit in mode A is $|1\rangle_A$ then this rotation is performed on mode B . This can be shown as:

$$\mathcal{N}_\alpha^+ | \alpha \rangle_B + | -\alpha \rangle_B \xrightarrow{\hat{R}_{\frac{\pi}{2}}} \mathcal{N}_\alpha^+ | i\alpha \rangle_B + | -i\alpha \rangle_B. \quad (5)$$

The final hybrid entangled state produced from this sequence of quantum logic gates is then that of Eq. 1.

This process can be shown as a quantum circuit as per Fig. 3:

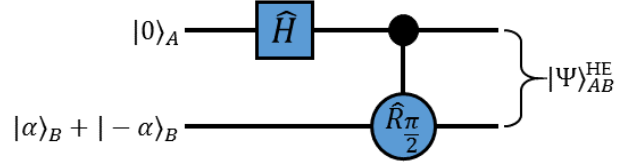


Figure 3: A quantum circuit which could be used to prepare the initial hybrid entangled states ($|\Psi\rangle_{AB}^{\text{HE}}$ and $|\Psi\rangle_{CD}^{\text{HE}}$, as given in Eq. 1) for our proposed entanglement swapping protocol, using a Hadamard gate (\hat{H}) and a controlled $\frac{\pi}{2}$ rotation gate ($\hat{R}_{\frac{\pi}{2}}$).

This circuit therefore demonstrates that these particular hybrid states can be produced using standard quantum operations.

2.3 Stage 2: Lossy Optical Modes

In any practical demonstration of this protocol, there will be intrinsic photonic losses that occur in the propagating modes (such as within optical fibres), and so we model these losses to investigate the tolerance of our protocol to this (see Stage 2 of Fig. 1).

To model photonic losses we combine the lossy modes (B and D) with beam-splitters of transmission T , along with input vacuum states in modes E_B and E_D ($|0\rangle_{E_B}$ and $|0\rangle_{E_D}$), for losses in modes B and D respectively, and then trace out the loss modes as lost to the environment. Therefore, by decreasing the value of T from unity we introduce greater levels of photonic loss in the system.

For now, we will consider the case in which the two beam-splitters ($BS_{B,E_B}^{T_B}$ and $BS_{D,E_D}^{T_D}$) induce equal amounts of loss between modes B and D , thus $T_B = T_D$. In Sec. 3 we discuss the more realistic circumstance in which $T_B \neq T_D$.

To demonstrate how we mathematically account for photonic losses, consider an arbitrary coherent state $|\beta\rangle_i$ of complex amplitude β in mode i , which we combine with a BS of transmission T_i , along with a vacuum state in mode j :

$$\begin{aligned} BS_{i,j}^{T_i} |\beta\rangle_i |0\rangle_j &= \\ \exp \left[\sqrt{T_i} \beta \hat{a}^\dagger - \sqrt{T_i} \beta^* \hat{a} \right] & \\ \times \exp \left[\sqrt{1-T_i} \beta \hat{b}^\dagger - \sqrt{1-T_i} \beta^* \hat{b} \right] & |0\rangle_i |0\rangle_j \\ &= |\sqrt{T_i} \beta\rangle_i |\sqrt{1-T_i} \beta\rangle_j, \end{aligned} \quad (6)$$

where \hat{a}^\dagger (\hat{b}^\dagger) and \hat{a} (\hat{b}) are the creation and annihilation operators for modes A and B , respectively.

The total quantum state of the ES protocol after inducing photonic losses is then described as:

$$|\Psi\rangle_{ABE_B CDE_D} = BS_{B,E_B}^{T_B} |\Psi\rangle_{AB}^{\text{HE}} |0\rangle_{E_B} \otimes BS_{D,E_D}^{T_D} |\Psi\rangle_{CD}^{\text{HE}} |0\rangle_{E_D}, \quad (7)$$

in which,

$$|\Psi\rangle_{ABE_B} = \frac{(\mathcal{N}_\alpha^+)^2}{2} \times \left[\left(|0\rangle_A (|\sqrt{T_B}\alpha\rangle_B |\sqrt{1-T_B}\alpha\rangle_{E_B} + |-\sqrt{T_B}\alpha\rangle_B |-\sqrt{1-T_B}\alpha\rangle_{E_B}) + |1\rangle_A (|i\sqrt{T_B}\alpha\rangle_B |i\sqrt{1-T_B}\alpha\rangle_{E_B} + |-i\sqrt{T_B}\alpha\rangle_B |-i\sqrt{1-T_B}\alpha\rangle_{E_B}) \right) \right], \quad (8)$$

and the above state is identical to that describing modes C , D and E_D .

2.4 Stage 3: 50:50 Beam-Splitter

Following the introduction of loss into the propagating modes (B and D), we then mix these modes at a 50:50 BS (as per Stage 3 of our protocol, outlined in Fig. 1). Consider now two arbitrary coherent states, of complex amplitudes α and η in modes i and j respectively - the 50:50 BS ($BS_{i,j}^{1/2}$) convention we use here can be shown mathematically as:

$$BS_{i,j}^{1/2} |\alpha\rangle_i |\eta\rangle_j = \left| \frac{\alpha - \eta}{\sqrt{2}} \right\rangle_i \left| \frac{\alpha + \eta}{\sqrt{2}} \right\rangle_j. \quad (9)$$

2.5 Stage 4: Detection Methods

After mixing the lossy modes B and D via use of a 50:50 BS, we then need to detect these quantum states (Stage 4, Fig. 1) to project their respective wave-functions, thus ensuring successful ES to modes A and C . We measure mode B via a projective vacuum state measurement, and mode D via balanced homodyne detection.

2.5.1 Vacuum State Detection

By ‘‘vacuum state measurement’’ we mean that to reveal the absence of a photon (therefore indicating a vacuum state) one could use a *perfect* photodetector, and upon not hearing the characteristic *click* of the detector, indicating the presence of one or more photons, it can be assumed that there is not a photon present [48].

To measure the presence of a vacuum, or lack thereof, we apply a positive-operator valued measure (POVM) described by the operator [49]:

$$\hat{P}_i^0 = |0\rangle_i \langle 0|, \quad (10)$$

where $|0\rangle_i$ represents a vacuum state in mode i . This POVM measurement can be calculated by application of this vacuum projector \hat{P}_i^0 onto a coherent state (as is required in our proposed ES protocol). For example, consider an arbitrary coherent state of complex amplitude γ in mode i as follows:

$$\begin{aligned} |0\rangle_i \langle 0|\gamma\rangle_i &= |0\rangle_i e^{-\frac{|\gamma|^2}{2}} \sum_{n=0}^{\infty} \frac{\gamma^n}{\sqrt{n!}} |n\rangle_i \langle 0|n\rangle_i \\ &= |0\rangle_i e^{-\frac{|\gamma|^2}{2}} \sum_{n=0}^{\infty} \frac{\gamma^n}{\sqrt{n!}} \delta_{n,0} = |0\rangle_i e^{-\frac{|\gamma|^2}{2}}, \end{aligned} \quad (11)$$

in which we have applied the Fock basis representation of the coherent state ($|\gamma\rangle_i = e^{-\frac{|\gamma|^2}{2}} \sum_{n=0}^{\infty} \frac{\gamma^n}{\sqrt{n!}} |n\rangle_i$), and we have made use of the Kronecker delta function, in which $\delta_{n,0} = 0$ for $n \neq 0$ and $\delta_{n,0} = 1$ for $n = 0$. We also highlight here that the application of this projective vacuum state measurement introduces an exponential dampening term of $e^{-\frac{|\gamma|^2}{2}}$, which is intrinsically important to the resultant performance of our proposed ES protocol, as will be discussed later.

After performing this projective vacuum measurement, our total quantum state is:

$$\hat{P}_B^0 |\Psi\rangle_{ABE_B CDE_D} = \sqrt{\mathcal{P}_0} |\Psi\rangle_{AE_B CDE_D}, \quad (12)$$

in which \mathcal{P}_0 is the success probability of the vacuum measurement (this will be discussed further in Subsec. 4.4). For clarity, we omit the state $|0\rangle_B$ on the right-hand side of Eq. 12 (and in further expressions), as this is the remaining state from the vacuum measurement operator (Eq. 10) after projecting mode B , and this will be used to project the complex conjugate of mode B when used to form the final density matrix.

2.5.2 Homodyne Measurement

Following the vacuum measurement of mode B , we proceed to measure mode D via balanced homodyne detection.

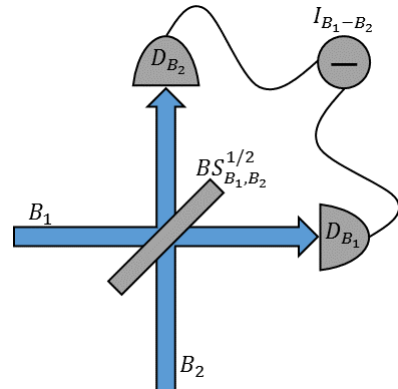


Figure 4: The two channel system undergoing homodyne detection, in which B_1 is the input signal (mode D in our ES protocol of Fig. 1), and mode B_2 is the local oscillator. $I_{B_1-B_2}$ is the intensity difference between the photodetectors D_{B_1} and D_{B_2} .

To perform balanced homodyne detection, the probe mode (mode B_1 as per Fig. 4) is mixed at a 50:50 BS with a strong coherent field $|\beta e^{i\theta}\rangle$, in which β is real, in mode B_2 (also referred to commonly as the local oscillator) of equal frequency, and photodetection is used to measure the outputs of both modes B_1 and B_2 [50–52], as shown in Fig. 4.

The intensity difference between the two photodetectors (D_{B_1} and D_{B_2}) is then calculated using the two mode operator $\hat{I}_{\hat{B}_1 - \hat{B}_2}$ as:

$$\hat{I}_{\hat{B}_1 - \hat{B}_2} = \hat{b}_1^\dagger \hat{b}_2 + \hat{b}_2^\dagger \hat{b}_1. \quad (13)$$

Setting the local oscillator mode to $\hat{b}_2 = \beta e^{i\theta}$ then yields the expectation value as:

$$\langle \hat{b}_1^\dagger \hat{b}_2 + \hat{b}_2^\dagger \hat{b}_1 \rangle = 2\beta \langle \hat{x}_\theta \rangle, \quad (14)$$

for $\hat{x}_\theta = \frac{1}{2}(\hat{b}_1 e^{-i\theta} + \hat{b}_1^\dagger e^{i\theta})$ [53], in which the phase of the quadrature to be measured is given by the phase θ of the local oscillator [54]. We adjust the phase angle such that $\hat{x}_{\theta \rightarrow 0} = \hat{x}$ and $\hat{x}_{\theta \rightarrow \pi/2} = \hat{p}$, thus giving the position and momentum operators, respectively, as:

$$\hat{x} = \frac{1}{2}(\hat{a} + \hat{a}^\dagger) \quad \text{and} \quad \hat{p} = \frac{i}{2}(\hat{a}^\dagger - \hat{a}), \quad (15)$$

in which the coherent state expectation values are:

$$\langle \hat{x} \rangle = \frac{1}{2}(\alpha + \alpha^*) \quad \text{and} \quad \langle \hat{p} \rangle = \frac{1}{2i}(\alpha^* - \alpha), \quad (16)$$

for $\alpha = \alpha_x + i\alpha_y$ and $\alpha^* = \alpha_x - i\alpha_y$.

Finally, the probability amplitude of a projective homodyne measurement on an arbitrary coherent state $|\alpha e^{i\phi}\rangle$ is determined by projecting with an \hat{x}_θ eigenstate, in which $\hat{x}_\theta |x_\theta\rangle = x_\theta |x_\theta\rangle$ [55]:

$$\begin{aligned} \langle x_\theta | \alpha e^{i\phi} \rangle = & \frac{1}{2^{-\frac{1}{4}} \pi^{\frac{1}{4}}} \exp \left[- (x_\theta)^2 + 2e^{i(\phi-\theta)} \alpha x_\theta \right. \\ & \left. - \frac{1}{2} e^{2i(\phi-\theta)} \alpha^2 - \frac{1}{2} \alpha^2 \right], \end{aligned} \quad (17)$$

where the subscript on x_θ is indicative of the angle in which the homodyne measurement is performed, and this angle can be accurately chosen through the phase of the local oscillator. We recognise here that homodyne detection is a routine and very accurate measurement technique used widely in optics as a means of measuring phase-dependent quantum phenomena [56–59].

The outcome of a homodyne measurement is a value x_θ of the continuous quadrature variable \hat{x}_θ , and the resultant homodyne measurement value is given by a probability distribution that comes from the modulus squared of the wave-function (as given in Eq. 17). For this work, we therefore define an *ideal*

homodyne measurement as the case when the resultant homodyne measurement value is at the maximum of the probability distribution, as indicated by the position and momentum phase space diagram of Fig. 5 (note that the states in this diagram have amplitudes of $\sqrt{2}\alpha$, which is a result of the 50:50 BS operation prior to this measurement).

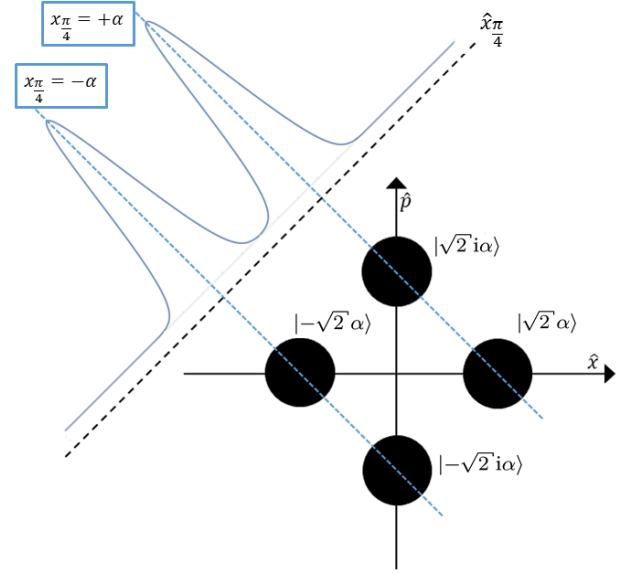


Figure 5: The position and momentum phase space occupied by two cat states $\mathcal{N}_\alpha^+(|\sqrt{2}\alpha\rangle + |-\sqrt{2}\alpha\rangle)$ and $\mathcal{N}_\alpha^+(|\sqrt{2}i\alpha\rangle + |-\sqrt{2}i\alpha\rangle)$, in which an $\hat{x}_{\pi/4}$ homodyne measurement yields a probability distribution exhibiting two peaks, centred at $x_{\pi/4} = \pm\alpha$.

Therefore, upon performing the homodyne measurement we have the total quantum state of:

$$\hat{\Pi}_{\text{HD}} |\Psi\rangle_{AE_B C D E_D} = |\Psi\rangle_{AE_B C E_D}, \quad (18)$$

in which $\hat{\Pi}_{\text{HD}} = |x_{\pi/4}\rangle_D \langle x_{\pi/4}|$ is the homodyne measurement projector, of measurement angle $\frac{\pi}{4}$. Again, as with the measurement of mode B (Eq. 12), we omit mode D on the right-hand side of this expression, as this is removed when forming the final state density matrix.

We select the angle of measurement $\theta = \frac{\pi}{4}$ such that we *quantum erase* information between certain peaks in the probability amplitude. To clarify, the purpose of the homodyne measurement in this scenario is to *indistinguishably* detect the coherent states, thus causing the output state to exhibit entanglement; the homodyne measurement outcome heralds the entangled state that is produced.

Considering the position and momentum of the cat states in Fig. 5, were we to measure along the $\hat{x}_{\pi/2}$ axis, for example, then we would only erase information between the two states along the momentum axis ($|\sqrt{2}i\alpha\rangle$ and $|-\sqrt{2}i\alpha\rangle$). This means that the output probability distribution would have three peaks, thus causing the remaining quantum state to be less entangled than for the circumstance in which we quantum erase information between

the states by an $\hat{x}_{\frac{\pi}{4}}$ measurement, as shown in Fig. 5. Of course, ideally one would perform this measurement with an angle such that there is only a single peak in the resultant probability distribution, however this is impossible for the case at hand.

A homodyne measurement along the $\hat{x}_{\frac{\pi}{4}}$ axis, as shown in Fig. 5 has two peaks centred at $x_{\frac{\pi}{4}} = \pm\alpha$, and so we use this result as our homodyne measurement outcome in establishing the final quantum state in this ES protocol. We emphasise that a homodyne measurement is a continuous quadrature measurement, and so realistically there is a range of outcome values in which x_{θ} may take (hence, as per Fig. 5, $x_{\frac{\pi}{4}} = \pm\alpha$ are the average *perfect* outcomes). Therefore, to investigate *imperfect* homodyne detection we need to allow for a resolution bandwidth about the expected measurement outcome value. The mathematical method for this was derived in [60], and we use this in determining the acceptance value of how large the resolution bandwidth can be, whilst still producing entangled qubits of reasonable fidelity.

Following the derivation detailed in [60], the imperfect homodyne measurement operator becomes:

$$\hat{\Pi}_{HD}(x_0, \Delta x) = \int_{x_0 - \frac{\Delta x}{2}}^{x_0 + \frac{\Delta x}{2}} |x_{\theta}\rangle \langle x_{\theta}| dx_{\theta}, \quad (19)$$

in which x_0 is the expected measured value and Δx is the resolution bandwidth around this measured value. Intuitively, in the limit of $\Delta x \rightarrow 0$ we should approach the perfect homodyne measurement scenario as before. This, in fact, is how we determine success probability for the homodyne measurement, however this will be discussed in detail in Subsec. 4.3.

For successful ES, as per this protocol, it is essential that one performs a vacuum state measurement on one propagating mode, and a homodyne measurement on the other - it was found that if two homodyne measurements, or two vacuum measurements, are performed on modes B and D then the resultant quantum state is a linear combination of all possible two qubit states, which is a product state and therefore exhibits no entanglement, and as such is of little use for further quantum communication/computation purposes.

We also note that we post-select the state prior to this measurement, conditional on the required vacuum projection outcome on mode B . That is to say, if we hear the photon detector *click* then we do not perform homodyne detection on mode D , but instead restart the entanglement swapping protocol again.

3 Modelling Unequal Photonic Losses

In a practical setting, the two propagating modes B and D will not exhibit the exact same levels of photonic losses. For example, different lengths of optical fibres correspond to varying levels of loss -

shorter fibre intrinsically exhibits lower losses. In fact, optical fibres of equal length may even exhibit differing photonic losses. There are also potential errors when coupling optical fibre to components, such as the 50:50 BS used to mix modes B and D , or fibre splices within these modes. Hence, even if the lengths of fibre are identical, slightly different optical coupling in the two modes could give a small mismatch in losses. We could even consider the free-space ES scenario, in which the path lengths of modes B and D differ, and as such would exhibit varying levels of loss.

As such, the two BSs used to model this loss theoretically ($BS_{B,E_B}^{T_B}$ and $BS_{D,E_D}^{T_D}$) will not have equal transmission coefficients - that is to say that $T_B \neq T_D$. We therefore now determine whether allowing for a small difference in the losses experienced in these modes, which we denote v , impacts the quality of the entangled state shared between Alice and Bob post-protocol.

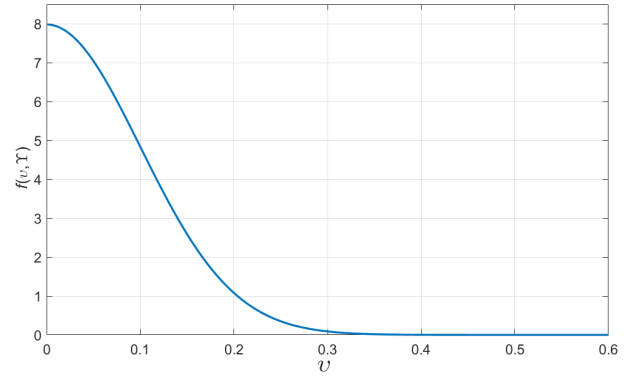


Figure 6: The one-sided (positive) Gaussian distribution for the unequal loss function ($f(v, \Upsilon)$), as a function of the (non-averaged) loss mismatch value v , of width $\Upsilon = 0.10$.

To avoid transmission coefficients exceeding unity (which is clearly unphysical), we parametrise our unequal loss parameter such that $T_B = T$ and $T_D = T - v$, in which $0 \leq T \leq 1$ and $0 \leq v \leq 1$. When allowing for this “loss mismatch”, our total quantum state, after the lossy BSs, is then:

$$\begin{aligned} |\Psi(v)\rangle_{ABE_B CDE_D} &= \frac{(\mathcal{N}_\alpha^+)^2}{2} \times \\ &\left[\left(|0\rangle_A (|\sqrt{T}\alpha\rangle_B |\sqrt{\gamma}\alpha\rangle_{E_B} \right. \right. \\ &\quad \left. \left. + |-\sqrt{T}\alpha\rangle_B |-\sqrt{\gamma}\alpha\rangle_{E_B} \right) \right. \\ &\quad \left. + |1\rangle_A (|i\sqrt{T}\alpha\rangle_B |i\sqrt{\gamma}\alpha\rangle_{E_B} \right. \\ &\quad \left. + |-i\sqrt{T}\alpha\rangle_B |-i\sqrt{\gamma}\alpha\rangle_{E_B} \right) \otimes \\ &\left[\left(|0\rangle_C (|\sqrt{T-v}\alpha\rangle_D |\sqrt{\gamma+v}\alpha\rangle_{E_D} \right. \right. \\ &\quad \left. \left. + |-\sqrt{T-v}\alpha\rangle_D |-\sqrt{\gamma+v}\alpha\rangle_{E_D} \right) \right. \\ &\quad \left. + |1\rangle_C (|i\sqrt{T-v}\alpha\rangle_D |i\sqrt{\gamma+v}\alpha\rangle_{E_D} \right. \\ &\quad \left. + |-i\sqrt{T-v}\alpha\rangle_D |-i\sqrt{\gamma+v}\alpha\rangle_{E_D} \right) \right], \quad (20) \end{aligned}$$

where $\gamma = 1 - T$. Of course, in the limit of $v = 0$ we return to the equal loss scenario.

As opposed to selecting a specific value for this loss mismatch, it is logical to explore an average over v by means of a one-sided (positive) Gaussian distribution (see Fig. 6), in which the width associated with this distribution corresponds to our *ensemble-averaged* loss mismatch value, which we denote Υ . Considering this value as an ensemble average means that an experimentalist performing this ES protocol could have in mind a threshold of Υ for which they would know to not allow the mismatch in the loss to fall below.

The function for this Gaussian profile is calculated as:

$$f(v, \Upsilon) = \sqrt{\frac{2}{\pi\Upsilon^2}} e^{-\frac{v^2}{2\Upsilon^2}}, \quad (21)$$

which is normalised for $\int_0^\infty f(v, \Upsilon) dv = 1$.

Therefore, the final state for our overall ES protocol, when accounting for unequal (averaged) losses between the propagating CV modes (B and D), and after having performed vacuum state detection and a homodyne measurement, is:

$$\bar{\rho}_{AE_BCE_D}(\Upsilon) = \int_0^\infty f(v, \Upsilon) \rho_{AE_BCE_D}(v) dv, \quad (22)$$

where $\rho_{AE_BCE_D}(v) = |\Psi(v)\rangle_{AE_BCE_D} \langle\Psi(v)|$.

Lastly, we trace out the lossy modes (E_B and E_D) as lost to the environment, using the coherent state to trace, thus giving our final density matrix as:

$$\text{Tr}_{E_B, E_D} [\bar{\rho}_{AE_BCE_D}(\Upsilon)] = \bar{\rho}_{AC}(\Upsilon), \quad (23)$$

which we use to determine all subsequent results presented throughout this work.

Due to the length of many of the mathematical expressions within this protocol, we do not include these in this work. We direct the reader to the work of [47] for an in-depth discussion, including all mathematical detail, of each step of this proposed protocol.

4 Results and Discussion

Having performed successful ES, as per the protocol outlined in the prior sections, the state which Alice and Bob share (in the ideal, no loss, perfect measurements limits) is a phase-rotated Bell state:

$$|\Phi^+(\alpha)\rangle_{AC} = \frac{1}{\sqrt{2}} \left(e^{-i\alpha^2} |00\rangle_{AC} + e^{+i\alpha^2} |11\rangle_{AC} \right), \quad (24)$$

and the orthogonal Bell state to this is:

$$|\Phi^-(\alpha)\rangle_{AC} = \frac{1}{\sqrt{2}} \left(e^{-i\alpha^2} |00\rangle_{AC} - e^{+i\alpha^2} |11\rangle_{AC} \right). \quad (25)$$

This phase in the ideal outcome state (Eq. 24) could be corrected for via a suitable quantum operation (i.e. a phase-space rotation), or tracked through the protocol which the post-entangled state is being used for, such that the outcome state would be the maximally entangled $|\Phi^+\rangle_{AC} = \frac{1}{\sqrt{2}}(|00\rangle_{AC} + |11\rangle_{AC})$ Bell state.

4.1 Fidelity

As the aim and purpose of our proposed ES protocol is to produce a specific Bell state of the highest quality (and therefore highest level of entanglement), the most useful measure of the quantum state shared between Alice and Bob is fidelity.

We calculate the fidelity (F) using the standard formula of:

$$F = \langle \Phi^+(\alpha) | \bar{\rho}_{AC}(\Upsilon) | \Phi^+(\alpha) \rangle, \quad (26)$$

in which $|\Phi^+(\alpha)\rangle = \frac{1}{\sqrt{2}} \left(e^{-i\alpha^2} |00\rangle + e^{+i\alpha^2} |11\rangle \right)$ is the desired protocol outcome, and $\bar{\rho}_{AC}(\Upsilon)$ is the final density matrix of our ES protocol, given in Eq. 23. In the limit in which our protocol outcome is identical to $|\Phi^+(\alpha)\rangle$ the fidelity is $F = 1$, and as the closeness of these quantum states the fidelity drops from unity and approaches zero.

Fig. 7 shows the fidelity against the phase-rotated Bell state, and the state orthogonal to this Bell state ($|\Phi^-(\alpha)\rangle$), as a function of the coherent state amplitude α of our final density matrix (Eq. 22), but in the limit of $\Upsilon = 0$ (i.e. the losses experienced in modes B and D are equal).

Firstly, we can see in Fig. 7 that the plot of fidelity against the $|\Phi^+(\alpha)\rangle$ state plateaus at unity for $T = 1$ and $\alpha \geq 2.3$. This confirms that in the ideal limit (i.e. no loss) we can indeed produce the maximally entangled $|\Phi^+(\alpha)\rangle$ Bell state, following our ES protocol. What is also evident in Fig. 7 is that in the limit of very large α , and for non-unity T the fidelity of both plots (for $|\Phi^+(\alpha)\rangle$ and $|\Phi^-(\alpha)\rangle$) tends to $F = 0.50$; in fact, this 50:50 mixture of both Bell states is a mixed state, and exhibits no entanglement, and so is undesirable as the protocol outcome.

Moreover, we can also see in Fig. 7 that as we increase the level of losses in modes B and D , the fidelity against the desired Bell state is lower for all α - correspondingly, the fidelity therefore increases for the orthogonal Bell state, indicating the increased level of mixing.

If we consider the plot of Fig. 8, in which we now allow for an averaged loss mismatch between modes B and D , we can see that increasing this loss mismatch value (Υ) merely causes the fidelity plots to plateau to $F = 0.50$ more rapidly as a function of α . In fact, this result is positive for the performance of this protocol - allowing for unequal losses between modes B and D does nothing more to impact the outcome of our protocol than simply increasing the level of equal losses between these modes.

Lastly, noticeable in both the equal loss and unequal loss plots (Figs. 7 and 8 respectively) is that there is a double peak present, for all values of T and Υ investigated (although we recognise that the second peak becomes less pronounced as T decreases and/or Υ increases).

Mathematically, this is a direct consequence from the numerous exponential terms that are present in the final density matrix describing the resultant two qubit matrix - we do not explicitly present this density matrix, as each of the matrix terms contains a vast number of complicated exponential terms, however, in Appendix A we include the final quantum state (prior to tracing out the lossy modes), for the equal loss scenario. We also direct the reader to [47] for the mathematical detail of each stage of this ES protocol, including the final state generated.

These exponential terms present in the equal loss case of Eq. 30 (which are also present in the unequal loss scenario) can be seen as somewhat competing with each other; instead of seeing a simple peak followed by a decay due to exponential dampening, as a result of the introduction of loss into our system, we see a dip which is a consequence of exponential interference. This dip becomes less pronounced as the level of loss increases (for example, in the $T = 0.95$, $\Upsilon = 0.10$ plot of Fig. 8) - this is due to the exponential dampening effect, dependent on the level of loss, having a stronger impact on the final density matrix compared to the smaller effect of exponential interference.

Of course, this too is a positive result, as it means that we have a wide acceptance window of the coherent state amplitudes to prepare our initial states in, whilst still giving a tolerable fidelity. The maximum fidelity value varies as a function of α , dependent on the level of loss considered: for $T = 0.97$ the second peak gives the maximum fidelity, and for $T \leq 0.96$, the first of these peaks gives the best out-

come state, as shown in Fig. 7.

Finally, we also plot the fidelity against the desired $|\Phi^+(\alpha)\rangle$ Bell state, as a function of both α and the averaged unequal loss value Υ , for $T = 1$, in Fig. 9.

The plot of Fig. 9 does not quite reach unity, even at the peak α value. The reason for this is that the numerical calculation cannot be evaluated for Υ very close to 0, as the Gaussian function (Fig. 6) then becomes a delta function (i.e. no longer a continuous spectrum as per Fig. 6, but instead is zero everywhere except for $v = 0$). Intrinsically, we expect that in the limit of $\Upsilon = 0$ we return to the results shown in the equal loss scenario (Fig. 7), and so we would indeed then expect the plot of Fig. 9 to reach, and plateau at, unity.

From Figs. 7, 8 and 9, we can conclude that we do not desire an averaged loss mismatch value of $\Upsilon > 0.10$, as this gives an unacceptably low fidelity ($F \leq 0.80$) for all α . We consider an acceptable fidelity result to be $F \geq 0.80$, as we could use any of the multitude of entanglement purification protocols available [61–65] to increase this fidelity to a sufficient level for further quantum communication/computation uses (i.e. to $F \geq 0.95$).

We acknowledge here that this limit we have for unequal losses $\Upsilon \leq 0.10$ to give an acceptable protocol output fidelity is not detrimental to the usefulness of our ES protocol: as previously stated, we refer to Υ as an average for unequal losses, as this variable is intended to reflect the practical perspective of running this protocol as an experiment, in which one would perhaps have a range of optical fibres, each of differing length, for example. It then follows that an averaged loss mismatch value of $\Upsilon > 0.10$ represents quite a large range of optical fibre lengths, and so it would be possible for an experimentalist to avoid unequal losses greater than this limit proposed in any case.

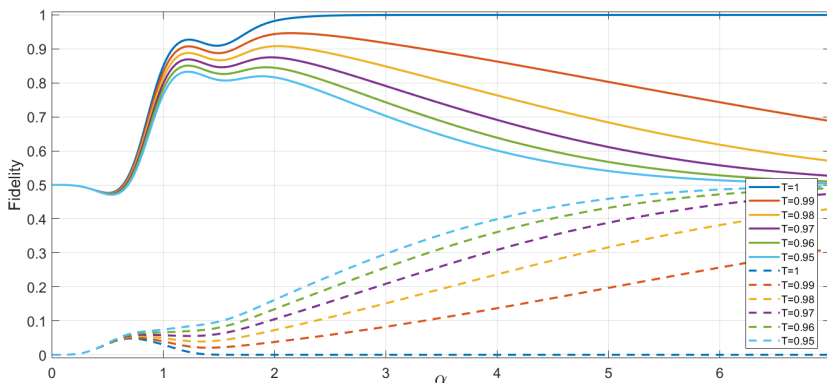


Figure 7: Fidelity against the $|\Phi^+(\alpha)\rangle$ (Eq. 24) Bell state (solid lines), and the orthogonal $|\Phi^-(\alpha)\rangle$ (Eq. 25) Bell state (dashed lines), as a function of the coherent state amplitude α , for the final state generated via our entanglement swapping protocol (Eq. 23), for varying levels of equal losses between modes B and D .

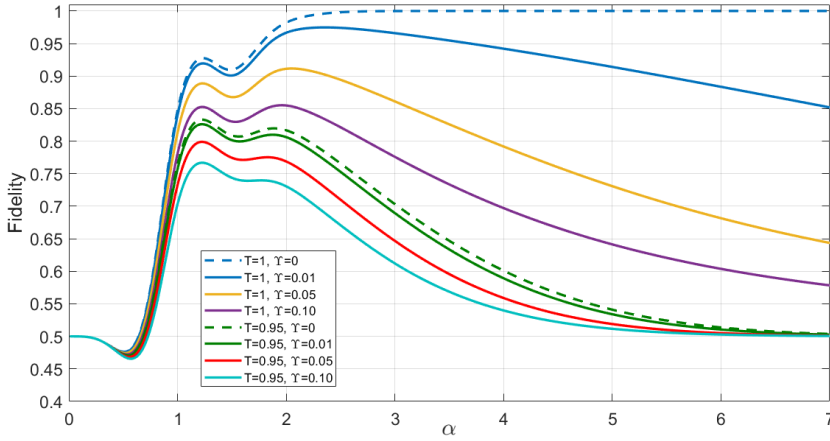


Figure 8: Fidelity against the $|\Phi^+(\alpha)\rangle$ (Eq. 24) Bell state, as a function of the coherent state amplitude α , for the final state generated via our entanglement swapping protocol (Eq. 23), for varying levels of equal loss, and averaged unequal loss (Υ).

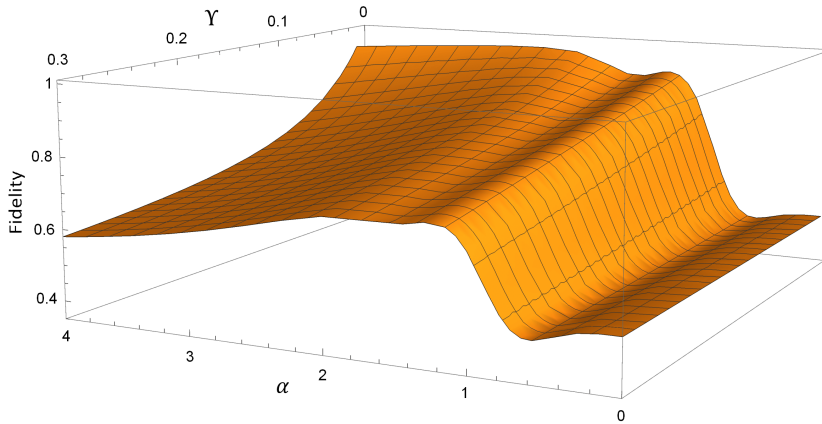


Figure 9: Fidelity against the $|\Phi^+(\alpha)\rangle$ (Eq. 24) Bell state, as a function of the coherent state amplitude α and the averaged unequal loss value Υ , for the final state generated via our entanglement swapping protocol (Eq. 23), for $T = 1$.

4.2 Imperfect Homodyne Detection

Thus far in the results and discussion, we have only analysed the scenario in which the homodyne measurement outcomes are the average *perfect* case. As briefly mentioned in Subsec. 2.5.2, to allow for imperfections in the homodyne measurement outcome, we follow the method outlined in [60], and consider a resolution bandwidth (Δx) around the average measurement outcome. The final state of our protocol when analysing homodyne imperfections is given in Appendix A Subsec. A.1, as a density matrix in Eq. 33.

Analysis of homodyne measurement imperfections are vital within this work, as no practical homodyne detector is able to measure with a bandwidth equal to $\Delta x \approx 0$. Hence, in this section we investigate the tolerance our protocol has to increasing this measurement bandwidth, whilst still producing a final state of acceptable fidelity. As we reduce Δx we are effectively allowing for fewer possible measurement outcomes when performing the protocol practically, and this is how we determine success probability of the homodyne measurement, as discussed in Subsec. 4.3.

Firstly, we plot the scenario of no loss (Fig. 10), to investigate the impact on output fidelity when increasing Δx to investigate the impact in the most idealised circumstance. From Fig. 10 we can see that the fidelity against the ideal Bell state ($|\Phi^+(\alpha)\rangle$) be-

gins to oscillate as we increase Δx . Intuitively we can conclude that these oscillations are present as a result of the numerous competing exponentials, which are dependent on Δx and also α within our final state (see Eq. 32).

Interestingly, this oscillatory behaviour is not present when observing higher values of loss ($T = 0.95$) as per Figs. 11 and 12. This is because the dampening exponentials introduced when accounting for losses, after having traced out the lossy modes, have a stronger influence on the final density matrix compared to the competing exponentials which produce the oscillations.

Promisingly, we find that introducing a relatively high level of detection imperfection ($\Delta x \leq 0.25$) does not significantly impact the resultant state fidelity against the ideal Bell state, even in the higher loss scenario. In fact, it is still evident that there is a peak α value as noticed in the previous fidelity plots discussed, and so if performing this practically one could take into account the known homodyne detector resolution bandwidth, and select the value of α which is likely to achieve the highest fidelity result.

Finally, we note that we do not show results for averaged unequal losses as these scale similarly to merely increasing the level of equal loss.

4.3 Homodyne Measurement Success Probability

Another important quantity to consider, in evaluating the performance of a protocol, is the success probability of the measurement schemes. As previously discussed, evaluating the homodyne detection resolution bandwidth Δx allows us to investigate the success probability of this measurement; increasing Δx means allowing for more outcome results of this measurement, and so we expect to see the success probability increase as Δx becomes larger.

Contrastingly, allowing for higher values of Δx impacts the resultant fidelity of the output state of the protocol, as discussed in Subsec. 4.2 - therefore we expect to witness a trade-off between the success of the protocol and the quality (fidelity) of the outcome. This is useful to understand, because in some cases the customer might wish to suffer a lower success rate to obtain high fidelity pairs.

To calculate the homodyne success probability we determine the modulus square of the normalised probability amplitudes (given by using the projector of Eq. 19 onto the coherent states present in mode D) to give us the probability distribution we integrate over, as:

$$|_D \langle x_{\frac{\pi}{4}} | \Psi \rangle_{A\varepsilon_B C D \varepsilon_D} |^2, \quad (27)$$

which then gives the success probability as:

$$\begin{aligned} \mathcal{P}_{Hom.}(\%) (\Upsilon) &= \int_0^\infty f(v, \Upsilon) \mathcal{N}_v \\ &\times \left(\int_{\frac{\mathcal{T}^+}{2} |\alpha| - \frac{\Delta x}{2}}^{\frac{\mathcal{T}^+}{2} |\alpha| + \frac{\Delta x}{2}} |_D \langle x_{\frac{\pi}{4}} | \Psi \rangle_{A\varepsilon_B C D \varepsilon_D} |^2 dx_{\frac{\pi}{4}} \right. \\ &\left. + \int_{-\frac{\mathcal{T}^+}{2} |\alpha| - \frac{\Delta x}{2}}^{-\frac{\mathcal{T}^+}{2} |\alpha| + \frac{\Delta x}{2}} |_D \langle x_{\frac{\pi}{4}} | \Psi \rangle_{A\varepsilon_B C D \varepsilon_D} |^2 dx_{\frac{\pi}{4}} \right) dv \times 100, \end{aligned} \quad (28)$$

where, $\mathcal{T}^+ = \sqrt{T} + \sqrt{T+v}$ and,

$$\begin{aligned} \mathcal{N}_v &= 1 / \left(4 + 8e^{-\frac{|\mathcal{T}^+ \alpha|^2}{4}} + 24e^{-\frac{|\mathcal{T}^+ \alpha|^2}{2}} + 8e^{-\frac{|\mathcal{T}^+ \alpha|^2}{4/3}} \right. \\ &\left. + 4e^{-|\mathcal{T}^+ \alpha|^2} + 8e^{-(2+i)|\mathcal{T}^+ \alpha|^2} + 8e^{-(2-i)|\mathcal{T}^+ \alpha|^2} \right)^{\frac{1}{2}}, \end{aligned} \quad (29)$$

is the normalisation. Although we show the full expression above for clarity, we do not present the results for equal and averaged unequal losses for homodyne success probability, as these scale as expected - incremental increases in the level of loss (be that equal or unequal) slightly lowers the success probability.

Fig. 13 shows the plot of the homodyne success probability $\mathcal{P}_{Hom.}(\%)$ as a function of α , for increasing Δx . Here we can see that for $\Delta x = 5.0$ the success probability is 100% for all α - this is because the resolution bandwidth at such a high value covers the entire spectrum of the cat state probability distribution. To further understand the plot of Fig. 13 it is useful to look at the probability distribution of the cat state equation (Eq. 27) for varying α , as per Fig. 14.

In Fig. 14, $\alpha = 0$ gives the vacuum state probability distribution, as expected. Contrastingly, if we look to higher values of α , then we see that for $\alpha = 2.0$ the two peaks of the probability distribution are almost entirely separated; this is the ideal scenario for successful homodyne detection, in which we have two outcome peaks to be measured (i.e. $x_{\frac{\pi}{4}} = \pm \alpha$ - see Fig. 5).

Moreover, when considering $\alpha = 1.0$ in Fig. 14, we can see that the width of this peak is broader than that of $\alpha = 0$. This is as a result of the vacuum states present in mode D , which are not ideal states for the homodyne measurement to project to, as measurement of these will not give an entangled output. These vacuum states are exponentially dampened as a function of α , and so it is not until $\alpha > 2.0$ when the contribution by the vacuum is reduced to a negligible amount.

Finally, we highlight that we indeed witness a trade-off between homodyne success probability and the output state fidelity. The success probability is optimum for very large Δx , however the output fidelity of the protocol would be very low in this scenario. Ideally, we would opt to use α values in the range of $1.0 \leq \alpha \leq 2.0$ and a measurement bandwidth of $\Delta x \leq 0.25$, which gives a success probability of around 10 - 15% in the no loss regime.

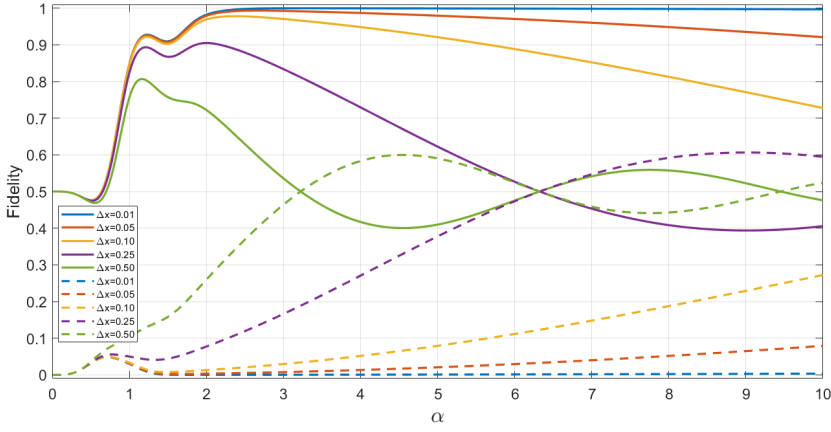


Figure 10: Fidelity against the $|\Phi^+(\alpha)\rangle$ (Eq. 24) Bell state (solid lines in plot) and the orthogonal $|\Phi^-(\alpha)\rangle$ (Eq. 25) Bell state (dotted lines in plot) as a function of α for the final state generated via our entanglement swapping protocol (Eq. 33), for $T = 1$ and varying homodyne measurement bandwidth Δx .

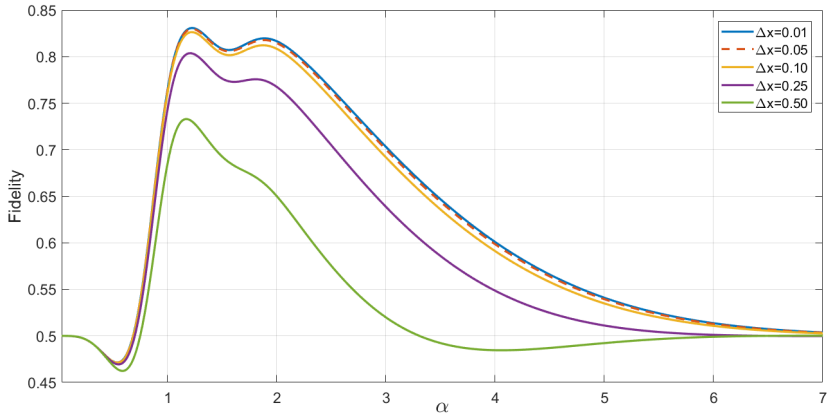


Figure 11: Fidelity against the $|\Phi^+(\alpha)\rangle$ (Eq. 24) Bell state as a function of α for the final state generated via our cat state entanglement swapping protocol (Eq. 33), for $T = 0.95$ and varying homodyne measurement bandwidth Δx .

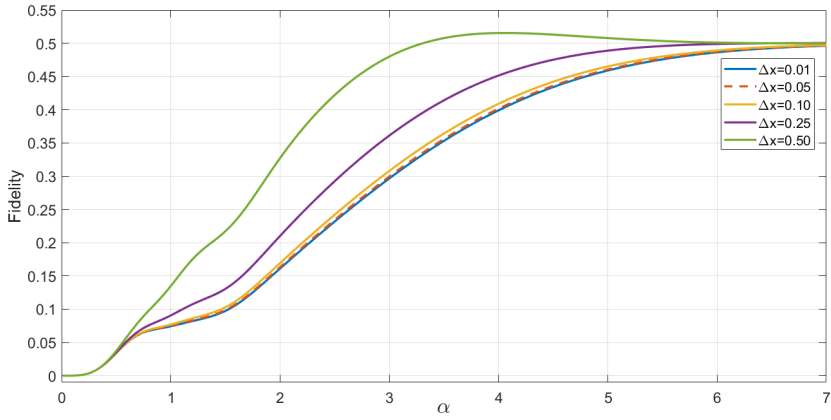


Figure 12: Fidelity against the $|\Phi^-(\alpha)\rangle$ (Eq. 25) Bell state as a function of α for the final state generated via our cat state entanglement swapping protocol (Eq. 33), for $T = 0.95$ and varying homodyne measurement bandwidth Δx .

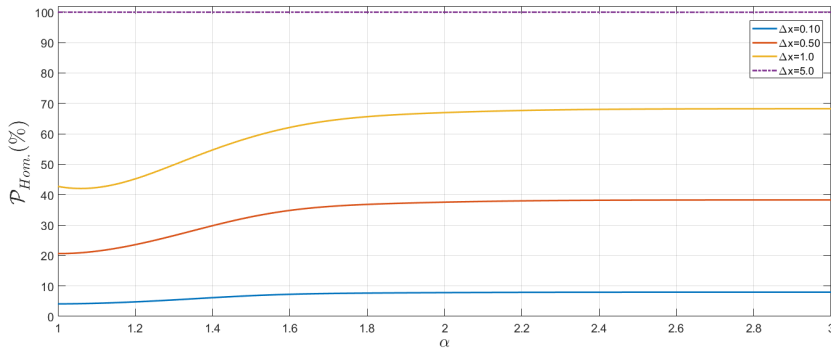


Figure 13: Success probability ($\mathcal{P}_{Hom.}(\%)$) of the homodyne measurement (Eq. 28), as a function of α , for varying homodyne measurement bandwidth Δx and $T = 1$.

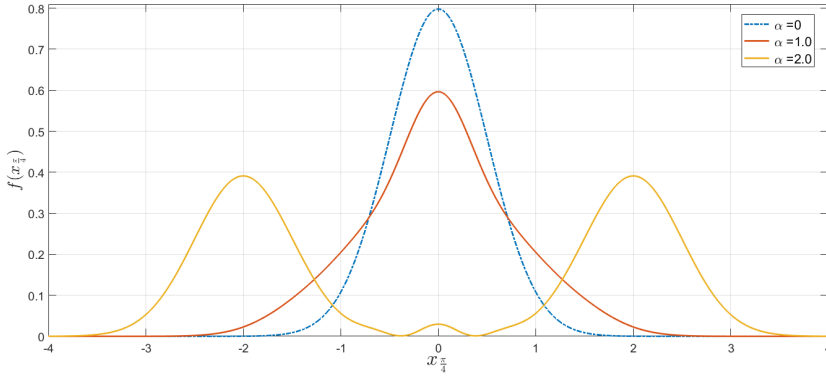


Figure 14: Probability distribution $f(x_{\frac{\pi}{4}})$ of the cat state equation (given by Eq. 27), as a function of $x_{\frac{\pi}{4}}$, for $\alpha = 0$, $\alpha = 1.0$ and $\alpha = 2.0$ (for no loss).

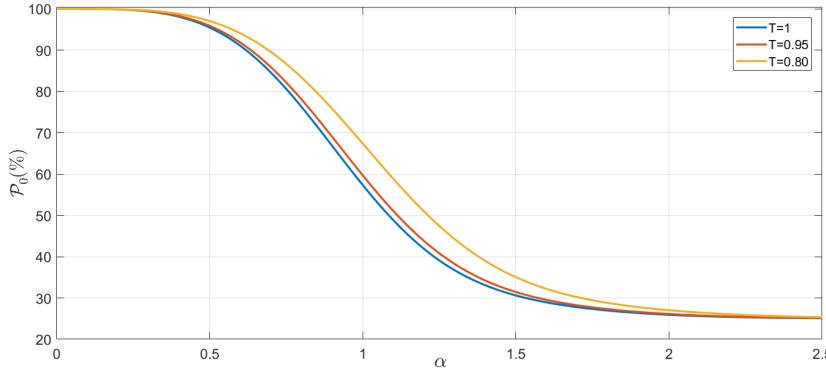


Figure 15: Success probability ($\mathcal{P}_0(\%)$) of the vacuum measurement, as a function of the coherent state amplitude α , for varying levels of equal losses between modes B and D . Note that we truncate the y -axis of the plot so that the range is from 20% \rightarrow 100%.

4.4 Vacuum Measurement Success Probability

We now discuss the success probability associated with the vacuum state measurement. Fig. 15 shows a plot of the vacuum measurement success probability (\mathcal{P}_0) as a function of the coherent state amplitude α . We only plot up to $\alpha = 2.5$, as this is the region we are primarily concerned with in our protocol, due to the fact that this is where our fidelity values peak as a function of α . Noticeably, we can see in Fig. 15 that for $\alpha = 0$, $\mathcal{P}_0 = 100\%$. Naturally, this is entirely expected, because at this value of $\alpha = 0$ all of these coherent states are in fact vacuum states, and so intrinsically any vacuum measurement here will always be performed with 100% success probability. More interestingly, we see that, for all values of loss covered in Fig. 15, all plots plateau at $\mathcal{P}_0 = 25\%$.

We also point out that although we have only considered equal losses between modes B and D in Fig. 15, the results are effectively identical when considering the same levels of unequal losses between these modes (as we noticed in the fidelity plots previously discussed).

Given the fidelity results presented in Figs. 7, 8 and 9, we can conclusively state that, for the levels of equal and unequal losses evaluated, we would desire coherent state amplitudes of $1.0 \leq \alpha \leq 2.0$, so as to achieve the peak fidelity results. In this region, however, the success probability begins to drop, and in fact at the higher end of this limit ($\alpha \approx 2.0$), we can see in Fig. 15 that the success probability is around $\mathcal{P}_0 = 25\%$.

This trade-off between fidelity and success probability is a common occurrence in quantum com-

munication schemes, and is something we must accept. Although success probability is undoubtedly significant when considering the practical implementation of our proposed ES protocol, we argue that high fidelity is far more important to aim for as opposed to better success probabilities; producing fewer pairs of higher fidelity quantum states is more useful for further quantum communication purposes, as opposed to producing a greater number of lower fidelity states.

5 Application in a Quantum Network

Thus far, we have shown that one could theoretically produce a highly entangled Bell state of fidelity $F \geq 0.80$, when allowing for photonic transmissions of $T = 0.95$ in the propagating modes (corresponding to losses of 5% \equiv 0.22 dB). Currently, the highest-performing low-loss fibre available exhibits losses of 0.149 dB/km [66], and so 5% loss in our protocol corresponds to maximum distances between Alice and Bob of 3.0 km (assuming the measurement apparatus to detect modes B and D is located precisely in the middle of Alice and Bob), whilst still being able to share an entangled Bell state of fidelity $F \geq 0.80$.

Of course, this limits our protocol to being used in short-distance entanglement distribution networks. Nevertheless, this scheme could be highly suitable for sharing entanglement between adjacent quantum computers within a future quantum network, possibly in a local area network (LAN), such as a university campus or research centre.

However, if we allow for higher levels of loss, and therefore lower resultant fidelity, we can intrinsically distribute entanglement to two parties further distanced apart. If we set our fidelity acceptance threshold to $F \geq 0.70$, then the losses we can tolerate in modes B and D are $T = 0.88$ (equivalent to 0.56 dB/km), allowing Alice and Bob to be located around 7.5 km apart if using ultra low-loss fibre of 0.149 dB/km. Moreover, if we allow our fidelity acceptance window to drop even further to $F \geq 0.60$, then we can allow for losses of $T = 0.84$, which corresponds to 0.76 dB, thus allowing Alice and Bob to share an entangled state whilst separated by an overall distance of 10.5 km.

Again, this still makes our proposed entanglement swapping protocol suitably only for relatively short LAN-type distances, however this comes at the advantage of being able to distribute highly entangled Bell states.

A Bell state of fidelity $F \leq 0.95$ is impractical for further uses with quantum computing, communications or information processing, and so allowing for further losses within our protocol means that a subsequent entanglement purification scheme would be required. Nevertheless, this is a common requirement for entanglement swapping protocols, and proposed quantum repeater networks use entanglement purification nodes as a fundamental part of the protocol.

Research into increasing the level of entanglement shared between two distant parties has been carried out extensively, and there exist a multitude of potential protocols which can increase Bell state fidelity from $F = 0.60$ to $F \geq 0.95$ [61–65]. Of course, in this circumstance this then requires one to use a higher number of lower fidelity pairs to produce one very high fidelity pair, although we argue that for the intended purpose of this protocol it is logical to sacrifice high bit rates to ensure that the entangled pairs delivered are of the best quality.

6 Conclusions

We summarise the key findings to this work as follows:

- Following our proposed ES protocol, we can produce a phase-rotated Bell state $|\Phi^+(\alpha)\rangle$ with fidelity of $F \geq 0.80$ for equal losses between modes B and D of $T \geq 0.95$ with an averaged loss mismatch value of $\Upsilon \geq 0.05$.

- Introduction of averaged unequal losses between the propagating modes does not significantly impact the protocol results, and in fact has no more of an effect than merely increasing the levels of equal losses between these channels.
- We witness a double peak in all fidelity plots, as a function of the coherent state amplitude α , and so we have a broader range of acceptable α values than in our previously proposed (coherent state superposition) protocol of [46], in which we witness only a single sharp peak.
- The protocol investigated in this work is also slightly more tolerant to induced losses than the work of [46].
- For the range of α which delivers a fidelity of $F \geq 0.80$, in the higher loss limits of ($T = 0.95$ and $\Upsilon = 0.05$) the success probability of the vacuum measurement is $\mathcal{P}_0 \approx 40\%$.
- We can allow for a fairly broad homodyne measurement bandwidth of $\Delta x \leq 0.50$, whilst still giving an entangled output state of respectable fidelity against the ideal case.

We reiterate that the phase present in the Bell state produced through our protocol, $|\Phi^+(\alpha)\rangle$, is not of detriment to the usefulness of this protocol in distributing entanglement to two parties; however in a practical implementation, this would require the customer to be informed of the exact phase present each time. As this phase is fixed by the value of α chosen, all post-entangled pairs received by the two parties will have the same phase.

Moreover, we conclude that this protocol is tolerant only to low levels of photonic losses, and so is more suitable for distributing entangled quantum states over a local area network between parties located 5-10 km apart, when followed by a suitable entanglement purification scheme. These entangled pairs of photons could then be used for further quantum communication purposes, or by adjacent quantum computing processors, which may require entanglement for communications or information processing [15].

7 Acknowledgements

The authors would like to thank Prof. Andrew Lord for useful discussions. We acknowledge support from EPSRC (EP/M013472/1).

A The Final State of the ES Protocol

The final state (prior to tracing out the lossy modes E_B and E_D) shared between Alice and Bob, for the scenario of equal losses between modes B and D , is:

$$\begin{aligned}
|\Psi\rangle_{AE_BCE_D} = & \mathcal{N} \left[|00\rangle_{AC} \left(\exp \left[(1-i)T\alpha^2 \right] |\gamma\alpha\rangle_{E_B} |\gamma\alpha\rangle_{E_D} + \exp \left[-(3-3i)T\alpha^2 \right] |-\gamma\alpha\rangle_{E_B} |-\gamma\alpha\rangle_{E_D} \right. \right. \\
& \left. \left. + e^{-T\alpha^2} \left(|\gamma\alpha\rangle_{E_B} |-\gamma\alpha\rangle_{E_D} + |-\gamma\alpha\rangle_{E_B} |\gamma\alpha\rangle_{E_D} \right) \right) \right. \\
& + e^{-\frac{T\alpha^2}{2}} |01\rangle_{AC} \left(\exp \left[T\alpha^2 \right] |\gamma\alpha\rangle_{E_B} |\gamma i\alpha\rangle_{E_D} + \exp \left[-2Ti\alpha^2 \right] |\gamma\alpha\rangle_{E_B} |-\gamma i\alpha\rangle_{E_D} \right. \\
& \left. + \exp \left[2Ti\alpha^2 \right] |-\gamma\alpha\rangle_{E_B} |\gamma i\alpha\rangle_{E_D} \right) + \exp \left[-3T\alpha^2 \right] |-\gamma\alpha\rangle_{E_B} |-\gamma i\alpha\rangle_{E_D} \\
& + e^{-\frac{T\alpha^2}{2}} |10\rangle_{AC} \left(\exp \left[T\alpha^2 \right] |\gamma i\alpha\rangle_{E_B} |\gamma\alpha\rangle_{E_D} + \exp \left[2Ti\alpha^2 \right] |\gamma i\alpha\rangle_{E_B} |-\gamma\alpha\rangle_{E_D} \right. \\
& \left. + \exp \left[-2Ti\alpha^2 \right] |-\gamma i\alpha\rangle_{E_B} |\gamma\alpha\rangle_{E_D} \right) + \exp \left[-3T\alpha^2 \right] |-\gamma i\alpha\rangle_{E_B} |-\gamma\alpha\rangle_{E_D} \\
& \left. + |11\rangle_{AC} \left(\exp \left[(i+1)T\alpha^2 \right] |\gamma i\alpha\rangle_{E_B} |\gamma i\alpha\rangle_{E_D} + \exp \left[-(3+3i)T\alpha^2 \right] |-\gamma i\alpha\rangle_{E_B} |-\gamma i\alpha\rangle_{E_D} \right. \right. \\
& \left. \left. + e^{-T\alpha^2} \left(|\gamma i\alpha\rangle_{E_B} |-\gamma i\alpha\rangle_{E_D} + |-\gamma i\alpha\rangle_{E_B} |\gamma i\alpha\rangle_{E_D} \right) \right) \right], \tag{30}
\end{aligned}$$

in which \mathcal{N} is the normalisation coefficient, $\gamma = \sqrt{1-T}$, and α is real. In the limit of large α (i.e. $\alpha > 2.5$), and no loss ($T = 1$), Eq. 30 reduces to the ideal Bell state outcome of $|\Phi^+(\alpha)\rangle = \frac{1}{\sqrt{2}} \left(e^{-i\alpha^2} |00\rangle + e^{+i\alpha^2} |11\rangle \right)$.

We note here that we do not explicitly include the equivalent final quantum state which includes averaged unequal losses between modes B and D , due to the length of this expression. We point the reader to the work of [47] for the mathematical detail.

A.1 Final State with Imperfect Homodyne Measurements

To derive the density matrix containing the homodyne bandwidth variable Δx , we begin with the equal loss state, immediately after the vacuum measurement and before the homodyne measurement, given by Eq. 12. We then apply the imperfect homodyne operator as per Eq. 19, for measurement angle $\theta = \frac{\pi}{4}$, such that:

$$\begin{aligned}
|\Psi\rangle_{A\varepsilon_BCD\varepsilon_D} = & \mathcal{N} \times \left[|00\rangle_{AC} \left[|\sqrt{2T}\alpha\rangle_D |\gamma|\alpha\rangle_{\varepsilon_B} |\gamma|\alpha\rangle_{\varepsilon_D} + |-\sqrt{2T}\alpha\rangle_D |-\gamma|\alpha\rangle_{\varepsilon_B} |-\gamma|\alpha\rangle_{\varepsilon_D} \right. \right. \\
& \left. \left. + e^{-T|\alpha|^2} |0\rangle_D \left(|\gamma|\alpha\rangle_{\varepsilon_B} |-\gamma|\alpha\rangle_{\varepsilon_D} + |-\gamma|\alpha\rangle_{\varepsilon_B} |\gamma|\alpha\rangle_{\varepsilon_D} \right) \right] \right. \\
& + e^{-\frac{T|\alpha|^2}{2}} |01\rangle_{AC} \left[|\sqrt{T}\alpha e^{\frac{i\pi}{4}}\rangle_D |\gamma|\alpha\rangle_{\varepsilon_B} |\gamma i|\alpha\rangle_{\varepsilon_D} + |\sqrt{T}\alpha e^{-\frac{i\pi}{4}}\rangle_D |\gamma|\alpha\rangle_{\varepsilon_B} |-\gamma i|\alpha\rangle_{\varepsilon_D} \right. \\
& \left. + |-\sqrt{T}\alpha e^{\frac{i\pi}{4}}\rangle_D |-\gamma|\alpha\rangle_{\varepsilon_B} |\gamma i|\alpha\rangle_{\varepsilon_D} + |-\sqrt{T}\alpha e^{-\frac{i\pi}{4}}\rangle_D |-\gamma|\alpha\rangle_{\varepsilon_B} |-\gamma i|\alpha\rangle_{\varepsilon_D} \right] \\
& + e^{-\frac{T|\alpha|^2}{2}} |10\rangle_{AC} \left[|\sqrt{T}\alpha e^{\frac{i\pi}{4}}\rangle_D |\gamma i|\alpha\rangle_{\varepsilon_B} |\gamma|\alpha\rangle_{\varepsilon_D} + |-\sqrt{T}\alpha e^{-\frac{i\pi}{4}}\rangle_D |\gamma i|\alpha\rangle_{\varepsilon_B} |-\gamma|\alpha\rangle_{\varepsilon_D} \right. \\
& \left. + |\sqrt{T}\alpha e^{\frac{i\pi}{4}}\rangle_D |-\gamma i|\alpha\rangle_{\varepsilon_B} |\gamma|\alpha\rangle_{\varepsilon_D} + |-\sqrt{T}\alpha e^{-\frac{i\pi}{4}}\rangle_D |-\gamma i|\alpha\rangle_{\varepsilon_B} |-\gamma|\alpha\rangle_{\varepsilon_D} \right] \\
& \left. + |11\rangle_{AC} \left[|\sqrt{2T}i\alpha\rangle_D |\gamma i|\alpha\rangle_{\varepsilon_B} |\gamma i|\alpha\rangle_{\varepsilon_D} + |-\sqrt{2T}i\alpha\rangle_D |-\gamma i|\alpha\rangle_{\varepsilon_B} |-\gamma i|\alpha\rangle_{\varepsilon_D} \right. \right. \\
& \left. \left. + e^{-T|\alpha|^2} |0\rangle_D \left(|\gamma i|\alpha\rangle_{\varepsilon_B} |-\gamma i|\alpha\rangle_{\varepsilon_D} + |-\gamma i|\alpha\rangle_{\varepsilon_B} |\gamma i|\alpha\rangle_{\varepsilon_D} \right) \right] \right], \tag{31}
\end{aligned}$$

$$\begin{aligned}
& \int_{x_0 - \frac{\Delta x}{2}}^{x_0 + \frac{\Delta x}{2}} |x_{\frac{\pi}{4}}\rangle_D \langle x_{\frac{\pi}{4}} | \Psi \rangle_{A\varepsilon_B C D \varepsilon_D} dx_{\frac{\pi}{4}} = \int_{\pm\sqrt{T}|\alpha| - \frac{\Delta x}{2}}^{\pm\sqrt{T}|\alpha| + \frac{\Delta x}{2}} |\Psi\rangle_{A\varepsilon_B C \varepsilon_D} dx_{\frac{\pi}{4}} = |\Psi(\Delta x)\rangle_{A\varepsilon_B C \varepsilon_D} \\
& = \int_{\pm\sqrt{T}|\alpha| - \frac{\Delta x}{2}}^{\pm\sqrt{T}|\alpha| + \frac{\Delta x}{2}} \mathcal{N} \frac{\exp[-(x_{\frac{\pi}{4}})^2]}{2^{-\frac{1}{4}} \pi^{\frac{1}{4}}} \\
& \quad \times \left[|00\rangle_{AC} \left(\exp\left[(1-i)2\sqrt{T}|\alpha|x_{\frac{\pi}{4}} + (i-1)T|\alpha|^2\right] |\gamma|\alpha\rangle_{\varepsilon_B} |\gamma|\alpha\rangle_{\varepsilon_D} \right. \right. \\
& \quad \quad \left. \left. + \exp\left[-(1-i)2\sqrt{T}|\alpha|x_{\frac{\pi}{4}} + (i-1)T|\alpha|^2\right] |-\gamma|\alpha\rangle_{\varepsilon_B} |-\gamma|\alpha\rangle_{\varepsilon_D} \right. \right. \\
& \quad \quad \left. \left. + e^{-T|\alpha|^2} \left(|\gamma|\alpha\rangle_{\varepsilon_B} |-\gamma|\alpha\rangle_{\varepsilon_D} + |-\gamma|\alpha\rangle_{\varepsilon_B} |\gamma|\alpha\rangle_{\varepsilon_D} \right) \right) \right. \\
& + e^{\frac{-T|\alpha|^2}{2}} |01\rangle_{AC} \left(\exp\left[2\sqrt{T}|\alpha|x_{\frac{\pi}{4}} - T|\alpha|^2\right] |\gamma|\alpha\rangle_{\varepsilon_B} |\gamma i|\alpha\rangle_{\varepsilon_D} + \exp\left[-2\sqrt{T}i|\alpha|x_{\frac{\pi}{4}}\right] |\gamma|\alpha\rangle_{\varepsilon_B} |-\gamma i|\alpha\rangle_{\varepsilon_D} \right. \\
& \quad \left. + \exp\left[2\sqrt{T}i|\alpha|x_{\frac{\pi}{4}}\right] |-\gamma|\alpha\rangle_{\varepsilon_B} |\gamma i|\alpha\rangle_{\varepsilon_D} + \exp\left[-2\sqrt{T}|\alpha|x_{\frac{\pi}{4}} - T|\alpha|^2\right] |-\gamma|\alpha\rangle_{\varepsilon_B} |-\gamma i|\alpha\rangle_{\varepsilon_D} \right) \\
& + e^{\frac{-T|\alpha|^2}{2}} |10\rangle_{AC} \left(\exp\left[2\sqrt{T}|\alpha|x_{\frac{\pi}{4}} - T|\alpha|^2\right] |\gamma i|\alpha\rangle_{\varepsilon_B} |\gamma|\alpha\rangle_{\varepsilon_D} + \exp\left[2\sqrt{T}i|\alpha|x_{\frac{\pi}{4}}\right] |\gamma i|\alpha\rangle_{\varepsilon_B} |-\gamma|\alpha\rangle_{\varepsilon_D} \right. \\
& \quad \left. + \exp\left[-2\sqrt{T}i|\alpha|x_{\frac{\pi}{4}}\right] |-\gamma i|\alpha\rangle_{\varepsilon_B} |\gamma|\alpha\rangle_{\varepsilon_D} + \exp\left[-2\sqrt{T}|\alpha|x_{\frac{\pi}{4}} - T|\alpha|^2\right] |-\gamma i|\alpha\rangle_{\varepsilon_B} |-\gamma|\alpha\rangle_{\varepsilon_D} \right) \\
& \quad \left. + |11\rangle_{AC} \left(\exp\left[(i+1)2\sqrt{T}|\alpha|x_{\frac{\pi}{4}} - (i+1)T|\alpha|^2\right] |\gamma i|\alpha\rangle_{\varepsilon_B} |\gamma i|\alpha\rangle_{\varepsilon_D} \right. \right. \\
& \quad \quad \left. \left. + \exp\left[-(1+i)2\sqrt{T}|\alpha|x_{\frac{\pi}{4}} - (i+1)T|\alpha|^2\right] |-\gamma i|\alpha\rangle_{\varepsilon_B} |-\gamma i|\alpha\rangle_{\varepsilon_D} \right. \right. \\
& \quad \quad \left. \left. + e^{-T|\alpha|^2} \left(|\gamma i|\alpha\rangle_{\varepsilon_B} |-\gamma i|\alpha\rangle_{\varepsilon_D} + |-\gamma i|\alpha\rangle_{\varepsilon_B} |\gamma i|\alpha\rangle_{\varepsilon_D} \right) \right) \right] dx_{\frac{\pi}{4}}, \tag{32}
\end{aligned}$$

in which we have set $x_0 = \pm\sqrt{T}|\alpha|$ in Eq. 32, as these are the ideal homodyne outcomes. Finally, to construct the final density matrix we merely trace out the lossy modes as before, giving the final state as:

$$\rho_{AC}(\Delta x) = \text{Tr}_{\varepsilon_B, \varepsilon_D} \left[\int_{\pm\sqrt{T}|\alpha| - \frac{\Delta x}{2}}^{\pm\sqrt{T}|\alpha| + \frac{\Delta x}{2}} |\Psi(\Delta x)\rangle_{A\varepsilon_B C \varepsilon_D} \langle \Psi(\Delta x) | dx_{\frac{\pi}{4}} \right]. \tag{33}$$

Note that we do not include the equivalent expressions for unequal losses and homodyne imperfections, due to the length of the derivation - however we again point the reader to [47] for the detail.

References

- [1] K. Boone et al. "Entanglement over global distances via quantum repeaters with satellite links". *Physical Review A* **91**, 5 (2015), p. 052325.
- [2] S. Pirandola and S. L. Braunstein. "Physics: Unite to build a quantum Internet". *Nature* **532**, 7598 (2016), pp. 169171.
- [3] J. Laurat. "On-demand entanglement could lead to scalable quantum networks". *Nature* **558**, 7709 (2018), pp. 192193.
- [4] A. K. Ekert. "Quantum cryptography based on Bells theorem". *Physical Review Letters* **67**, 6 (1991), pp. 661663.
- [5] H. Singh, D. Gupta, and A. Singh. "Quantum Key Distribution Protocols: A Review". *IOSR Journal of Computer Engineering* **16**, (2014), pp. 0109.
- [6] Y. Cao et al. "Entanglement-based quantum key distribution with biased basis choice via free space". *Optics Express* **21**, 22 (2013), p. 27260.
- [7] J. Yin et al. "Satellite-to-Ground Entanglement-Based Quantum Key Distribution". *Physical Review Letters* **119**, 20 (2017), p. 200501.
- [8] M. Nadeem and N. U. Ain. "Secure and authenticated quantum secret sharing". *arXiv:1506.08558 [quant-ph]* (2015).
- [9] T.-Y. Wang et al. "Security of a kind of quantum secret sharing with entangled states". *Scientific Reports* **7**, 1 (2017), p. 2485.
- [10] I. Kogias et al. "Unconditional security of entanglement-based continuous-variable quantum secret sharing". *Physical Review A* **95**, 1 (2017), p. 012315.
- [11] W. Dur et al. "Quantum repeaters based on entanglement purification". *Physical Review A* **59**, 1 (1999), pp. 169181.
- [12] P. van Loock et al. "Hybrid Quantum Repeater Using Bright Coherent Light". *Physical Review Letters* **96**, 24 (2006), p. 240501.
- [13] J. Dias and T. C. Ralph. "Quantum repeaters using continuous-variable teleportation". *Physical Review A* **95**, 2 (2017), p. 022312.

- [14] F. Furrer and W. J. Munro. "Repeaters for continuous-variable quantum communication". *Physical Review A* **98**, 3 (2018), p. 032335.
- [15] C. H. Bennett and D. P. DiVincenzo. "Quantum information and computation". *Nature* **404**, 6775 (2000), pp. 247255.
- [16] P. Arrighi and L. Salvail. "Blind Quantum Computation". *International Journal of Quantum Information* **04**, 05 (2006), pp. 883898.
- [17] H. J. Briegel et al. "Measurement-based quantum computation". *Nature Physics* **5**, 1 (2009), pp. 1926.
- [18] A. Saxena, K. Thapliyal, and A. Pathak. "Continuous variable controlled quantum dialogue and secure multiparty quantum computation". *arXiv:1902.00458 [quant-ph]* (2019).
- [19] C. H. Bennett et al. "Teleporting an unknown quantum state via dual classical and Einstein-Podolsky-Rosen channels". *Physical Review Letters* **70**, 13 (1993), pp. 18951899.
- [20] M. D. Barrett et al. "Deterministic quantum teleportation of atomic qubits". *Nature* **429**, 6993 (2004), pp. 737739.
- [21] R. Ursin et al. "Quantum teleportation across the Danube". *Nature* **430**, 7002 (2004), pp. 849849.
- [22] T. Herbst et al. "Teleportation of entanglement over 143 km". *Proceedings of the National Academy of Sciences of the United States of America* **112**, 46 (2015), pp. 142025.
- [23] A. Shaham et al. "Entanglement dynamics in the presence of controlled unital noise". *Scientific Reports* **5**, 1 (2015), p. 10796.
- [24] F. Xu et al. "Measurement-Device-Independent Quantum Cryptography". *IEEE Journal of Selected Topics in Quantum Electronics* **21**, 3 (2015), pp. 148158.
- [25] W.-Y. Hwang, H.-Y. Su, and J. Bae. "Improved measurement-device-independent quantum key distribution with uncharacterized qubits". *Physical Review A* **95**, 6 (2017), p. 062313.
- [26] Z.-R. Zhou et al. "Measurement-Device-Independent Quantum Secure Direct Communication". *arXiv:1805.07228 [quant-ph]* (2018).
- [27] I. Jeon and H. Jeong. "Measurement-device-independent and arbitrarily loss-tolerant verification of quantum steering". *Physical Review A* **99**, 1 (2019), p. 012318.
- [28] M. Zukowski et al. "Event-ready-detectors Bell experiment via entanglement swapping". *Physical Review Letters* **71**, 26 (1993), pp. 42874290.
- [29] S. Giacomini et al. "Active teleportation of a quantum bit". *Physical Review A* **66**, 3 (2002), p. 030302.
- [30] T. Jennewein et al. "Experimental Nonlocality Proof of Quantum Teleportation and Entanglement Swapping". *Physical Review Letters* **88**, 1 (2001), p. 017903.
- [31] R. Kaltenbaek et al. "High-fidelity entanglement swapping with fully independent sources". *Physical Review A* **79**, 4 (2009), p. 040302.
- [32] X. Jia et al. "Experimental Demonstration of Unconditional Entanglement Swapping for Continuous Variables". *Physical Review Letters* **93**, 25 (2004), p. 250503.
- [33] N. Takei et al. "High-Fidelity Teleportation beyond the No-Cloning Limit and Entanglement Swapping for Continuous Variables". *Physical Review Letters* **94**, 22 (2005), p. 220502.
- [34] H. Jeong et al. "Generation of hybrid entanglement of light". *Nature Photonics* **8**, 7 (2014), pp. 564569.
- [35] A. Orioux and E. Diamanti. "Recent advances on integrated quantum communications". *Journal of Optics* **18**, 8 (2016), p. 083002.
- [36] E. Diamanti and A. Leverrier. "Distributing Secret Keys with Quantum Continuous Variables: Principle, Security and Implementations". *Entropy* **17**, 12 (2015), pp. 60726092.
- [37] J. B. Brask et al. "Hybrid Long-Distance Entanglement Distribution Protocol". *Physical Review Letters* **105**, 16 (2010), p. 160501.
- [38] Y. Lim et al. "Loss-resilient photonic entanglement swapping using optical hybrid states". *Physical Review A* **6**, 94 (2016), pp. 5055.
- [39] S. Takeda et al. "Entanglement Swapping between Discrete and Continuous Variables". *Physical Review Letters* **114**, 10 (2015), p. 100501.
- [40] O. Morin et al. "Remote creation of hybrid entanglement between particle-like and wave-like optical qubits". *Nature Photonics* **8**, 7 (2014), pp. 570574.
- [41] C. C. Gerry. "Generation of optical macroscopic quantum superposition states via state reduction with a Mach-Zehnder interferometer containing a Kerr medium". *Physical Review A* **59**, 5 (1999), pp. 40954098.

- [42] H. Jeong. "Using weak non-linearity under decoherence for macroscopic entanglement generation and quantum computation". *Physical Review A* **72**, 3 (2005), p. 034305.
- [43] P. van Loock et al. "Hybrid Quantum Repeater Using Bright Coherent Light". *Physical Review Letters* **96**, 24 (2006), p. 240501.
- [44] K. Nemoto and W. J. Munro. "Nearly Deterministic Linear Optical Controlled-NOT Gate". *Physical Review Letters* **93**, 25 (2004), p. 250502.
- [45] S. Li et al. "Experimentally feasible generation protocol for polarized hybrid entanglement". *Physical Review A* **98**, 2 (2018), p. 022334.
- [46] R. C. Parker et al. "Hybrid photonic loss resilient entanglement swapping". *Journal of Optics* **19**, 10 (2017), p. 104004.
- [47] R. C. Parker. "A Loss Resilient Entanglement Swapping Protocol using Non-Classical States of Light". PhD thesis. University of York (2018).
- [48] C. C. Gerry. "Heisenberg-limit interferometry with four-wave mixers operating in a nonlinear regime". *Physical Review A* **61**, 4 (2000), p. 043811.
- [49] J. Joo, T. Rudolph, and B. C. Sanders. "A heralded two-qutrit entangled state". *Journal of Physics B: Atomic, Molecular and Optical Physics* **42**, 11 (2009), p. 114007.
- [50] M. O. Scully and M. S. Zubairy. "Quantum optics". Cambridge University Press (1997).
- [51] S. D. Barrett et al. "Symmetry analyzer for nondestructive Bell-state detection using weak nonlinearities". *Physical Review A* **71**, 6 (2005), p. 060302.
- [52] S. Suzuki et al. "Practical purification scheme for decohered coherent-state superpositions via partial homodyne detection". *Physical Review A* **73**, 4 (2006), p. 042304.
- [53] C. C. Gerry and P. L. Knight. "Introductory quantum optics". Cambridge University Press (2005).
- [54] A. I. Lvovsky and M. G. Raymer. "Continuous-variable optical quantum-state tomography". *Reviews of Modern Physics* **81**, 1 (2009), pp. 299332.
- [55] C. W. Gardiner and P. Zoller. "Quantum noise: a handbook of Markovian and non-Markovian quantum stochastic methods with applications to quantum optics". Springer (2004).
- [56] J. W. Noh, A. Fougères, and L. Mandel. "Measurement of the quantum phase by photon counting". *Physical Review Letters* **67**, 11 (1991), pp. 14261429.
- [57] D. T. Smithey et al. "Measurement of the Wigner distribution and the density matrix of a light mode using optical homodyne tomography: Application to squeezed states and the vacuum". *Physical Review Letters* **70**, 9 (1993), pp. 12441247.
- [58] D. T. Smithey et al. "Complete experimental characterization of the quantum state of a light mode via the Wigner function and the density matrix: application to quantum phase distributions of vacuum and squeezed-vacuum states". *Physica Scripta* **T48** (1993), pp. 3544.
- [59] T. Lipfert, J. Sperling, and W. Vogel. "Homodyne detection with on-off detector systems". *Physical Review A* **92**, 5 (2015), p. 053835.
- [60] A. Laghaout et al. "Amplification of realistic Schrödinger-cat-state-like states by homodyne heralding". *Physical Review A* **87**, 4 (2013), p. 043826.
- [61] J.-W. Pan et al. "Entanglement purification for quantum communication". *Nature* **410**, 6832 (2001), pp. 10671070.
- [62] J.-W. Pan et al. "Experimental entanglement purification of arbitrary unknown states". *Nature* **423**, 6938 (2003), pp. 417422.
- [63] X.-L. Feng, S.-Q. Gong, and Z.-Z. Xu. "Entanglement purification via controlled controlled NOT operations". *Physics Letters A* **271**, 1-2 (2000), pp. 4447.
- [64] C. Cai, L. Zhou, and Y.-B. Sheng. "Fast multi-copy entanglement purification with linear optics". *Chinese Physics B* **24**, 12 (2015), p. 120306.
- [65] S.-S. Zhang et al. "Multi-copy entanglement purification with practical spontaneous parametric down conversion sources". *Chinese Physics B* **26**, 6 (2017), p. 060307.
- [66] Y. Kawaguchi et al. "Ultra low-loss pure silica core fiber". *SEI Technical Review*, **80** (2015), pp. 5055.